Supplementary Material

The Atmospheric Oxidizing Capacity in China: Part 1. Roles of different photochemical processes

Jianing Dai[a], Guy P. Brasseur[a,e,f], Mihalis Vrekoussis[b,g,h], Maria Kanakidou [b,d], Kun Qu[b], Yijuan Zhang[b], Hongliang Zhang[c], Tao Wang[f]

[a] Environmental Modelling Group, Max Planck Institute for Meteorology, Hamburg, 20146, Germany
[b] Institute of Environmental Physics (IUP), University of Bremen, Bremen, 28359, Germany
[c] Department of Environmental Science and Engineering, Fudan University, 200433, China
[d] Environmental Chemical Processes Laboratory, Department of Chemistry, University of Crete, Heraklion, 71003, Greece
[e] National Center for Atmospheric Research, Boulder, Colorado, 80307, USA
[f] Department of Civil and Environmental Engineering, The Hong Kong Polytechnic University, Hong Kong, China
[g] Center of Marine Environmental Sciences (MARUM), University of Bremen, Germany
[h] Climate and Atmosphere Research Center (CARE-C), The Cyprus Institute, Nicosia, Cyprus

Correspondence to: Guy P. Brasseur (guy.brasseur@mpimet.mpg.de)

Model validation. Figure S1 shows the spatial distribution of the calculated monthly average surface maximum daily 8-hour average (MDA8) ozone, as well as the monthly mean concentrations of NO_2, CO, and $PM_{2.5}$. A statistical evaluation of the surface concentration of these air pollutants is provided in Table S3. Our model matches well with the spatial distribution of MDA8 ozone (Figure S1a, b) in both January and July. High values of the correlation coefficient ($R > 0.85$) and low values of the mean bias (MB) are indicative of good model performance. An overestimation of ozone is simulated in central and western China in July, which is related to the underestimation of NO_2 in these areas (Figure S1 c, d). A comparison between the diurnal variations of the model and measured mixing ratios of NO_2 (Figure S2) and ozone (Figure S3) is provided in four large metropolitan areas for January and July. The agreement is generally good in the case of NO_2. The model, however, tends to overestimate the NO_2 concentrations during winter, specifically in Beijing and Shanghai. In the case of ozone, the agreement is rather good in the summer, but the model underestimates the urban concentrations during winter. An underestimation of the O_3/NO_2 ratio indicates an underestimation of the NO_2 photolysis or an overestimation of the HO_2 concentration.

As shown in Figure S1e-h, both CO and $PM_{2.5}$ are overestimated in the urban areas of northern and central China. This bias can be partially explained by the uncertainties in the adopted emissions and chemicals boundary (Dai et al., 2020).

Surface mixing ratios for NO, HONO, and formaldehyde (HCHO) are displayed in Figure S4 and the comparison of the calculated concentrations with measured data in four urban and four remote sites are shown in Figures S7 and S8. The spatial distribution of NO and HONO have a similar pattern, with high concentration values found in the northern urban areas, especially during winter. The HONO concentration is highest during nighttime, which is opposite to the case of NO, whose concentration is maximum during daytime. The maximum values of the calculated HONO concentrations are found in urban and rural areas within the range of 2.4-3.00 ppbv and 0.75 - 3.00 ppbv in January and July, respectively (Figure S8). A comparison between the values of HONO derived from local observations is compared with model estimates in Table S4. High values of surface HCHO are derived in the southern part of China, especially in summer. This region with high values of solar radiation and temperature exhibits high concentrations of isoprene (Figure S6b), which favors the formation of HCHO (Wang et al., 2021). Our calculated concentration of HCHO is consistent with the measured value of 6.5 ppbv in the summer at Chengdu (Yang et al., 2021) and of 5.8-6.8 and 4.9 ppbv in the Fall at Heshan (Tan et al., 2017) and Shenzhen (Yang et al., 2022), respectively.

The surface mixing ratios of OH, HO_2, and NO_3 are in Figure S5. During winter, the high concentrations of OH are distributed over the South China Sea and along the southern coast of the country; in summer, the highest values are found in the North China Plain area and along ship tracks in the East China Sea. These distributions are partially relevant to the seasonal variations of

water vapor and solar radiation and the distribution of concentrations of isoprene (Figure S4), NO (Figure S7), and HONO (Figure S8). In Beijing, the peak concentrations of calculated OH and HO_2 are 1.5×10^6 cm^{-3} and 1.0×10^7 cm^{-3} in winter and 1.2×10^7 cm^{-3} and 1.0×10^9 cm^{-3} in summer (Figure S10 and S9), respectively. These values are consistent with the observed peak concentrations of OH and HO_2 of 1.5×10^6 - 2.0×10^6 cm^{-3} and of 3.0×10^7 - 4.0×10^7 cm^{-3} in winter (Ma et al., 2019) and of 8.0×10^6 - 9.0×10^6 cm^{-3} and 3×10^8 - 15×10^8 cm^{-3} in summer (Yang et al., 2021) reported in this area. In Guangzhou sites, the maximum concentration of OH and HO_2 is 10.0×10^6 cm^{-3} and 7.0×10^8 cm^{-3} in summer, which is slightly higher than the peak value of 4.5×10^6 cm^{-3} and 4.0×10^8 cm^{-3} measured in autumn at Shenzhen (Yang et al., 2022). In Chengdu, the maximum concentrations of OH and HO_2 measured during summertime are 1.0×10^7 cm^{-3} and 1.0×10^9 cm^{-3}, respectively, which is also consistent with our calculated level (1.5×10^7 cm^{-3} and 0.8×10^9 cm^{-3}) (Yang et al., 2021).

As NO_3 can be rapidly photolyzed during the daytime, high concentrations of this radical are found during nighttime. Nitrate is formed from the reaction between NO_2 and O_3 (Brown and Stutz, 2012). The calculated concentrations of NO_3 radical are highest in January, specifically in northern China, and in July along the ship tracks in the sea near the coast of southern China. The highest calculated concentrations of nighttime NO_3 are found at the Wangdu site (1.2×10^9 cm^{-3}) and at the Hok Tsui site (4.5×10^8 cm^{-3}) in January and July (Figure S11), respectively. There is only a very small number of NO_3 measurements that are currently reported in China. However, Wang et al., (2023) have recently highlighted the increasing role of the NO_3 radical for the nighttime oxidation capacity in China, specifically during the 2014 – 2019 period.

The spatial distribution of the aerosol surface area density, shown in Figure S12, is an important parameter determining the rate at which heterogeneous reactions proceed. In the eastern plain of China, the calculated values are substantially higher in January by 1×10^{-5} - 2×10^{-5} cm^2/cm^3 than in June by 0.2×10^{-5} - 0.5×10^{-5} cm^2/cm^3, which is consistent with the observed seasonal variation of the aerosol burden. The calculations of this parameter are based on the concentration of aerosol calculated in our model (Zaveri et al., 2008). Since the calculated $PM_{2.5}$ concentration appears to be slightly overestimated, the aerosol surface area density used to calculate the aerosol uptake may be overestimated.

Table S1. List of peroxy radicals (RO_2), volatile organic compounds (VOCs), and aerosol species in the MOZART-MOSAIC mechanism in the WRF-Chem model.

		Species
RO_2 (Emmons et al., 2010)		CH3O2, EO2, C2H5O2, PO2, CH3CO3, C3H7O2, RO2, ENEO2, ALKO2, MEKO2, ISOPO2, MACRO2, MCO3, PHENO2, C6H5O2, BENZO2, MALO2, BZOO, ACBZO2, TOLO2, DICARBO2, MDIALO2, XYLOLO2, XYLENO2, TERPO2, TERP2O2, NTERPO2, XO2, MBOO2, HMPROPO2, MBONO3O2
VOCs (Emmons et al., 2010)	Alkanes	C2H6, C3H8, BIGALK
	Alkenes	C2H4, C3H6, BIGENE, ISOPR, APIN, BPIN, LIMON
	Aromatics	BENZENE, TOLUNE, XYLENE, CRESOL
	Alkyne	C2H2
	Oxidized VOCs	HCHO, CH3CHO, POOH, CH3COOOH, PAN, MPAN, MACR, MVK, C2H5OOH, C3H7OOH, ROOH, CH3COCH3, CH3COCHO, XOOH, ONIT, ONITR, ISOPOOH, HYAC, GLYALD, MEK, BIGALD, GLYOXAL, ALKOOH, MEKOOH, TOLOOH, PHENOL, BEPOMUC, TEPOMUC, BIGALD1, BIGALD2, BIGALD3, BIGALD4, MBOOOH, HMPROP, TERPROD1, TERPROD2, TERPOOH, CH3OOH, MACROOH, PHENOOH, C6H5OOH, BENZOOH, BZOOH, BZALD, XYLOLOOH, XYLENOOH, TERP2OOH, CH3COOH, HYDRALD, CH3OH, C2H5OH, HCOOH, HOCH2OO
	Others	CH4
Aerosol species (Zaveri et al., 2008)		NA^+, NH_4^+, Cl^-, SO_4^{2-}, NO_3^-, OIN, OC, BC, SOA

Table S2. Physical modules used in model simulations

Atmospheric process	Scheme
Cloud microphysics	Morrison double moment (Morrison et al., 2005)
Cumulus parameterization	Grell 3D Ensemble Scheme (Grell and Dévényi., 2002)
Land-surface physics	Noah Land Surface Model (Chen and Dudhia., 2001)
Longwave radiation	RRTM scheme (Mlawer et al., 1997)
Shortwave radiation	RRTM scheme (Mlawer et al., 1997)
Planetary boundary layer	Yonsei University PBL (Hong et al., 2006)
Photolysis	Madronich Fast Tropospheric Ultraviolet-Visible (FTUV) (Madronich et al., 1987., Tie et al., 2003)

Table S3. Statistical analysis of key quantities that characterize the surface concentrations of air pollutants averaged over the entire geographical area of China for January and July.

	SIM		OBS		Bias		R		NMB		NME		RMSE	
	Jan.	July	Jan.	July	Jan.	July	Jan.	July	Jan.	July	Jan.	July	Jan.	July
Ozone ($\mu g\ m^{-3}$)	47.8	76.4	41.3	72.5	6.5	3.6	0.9	0.9	0.2	0.1	0.2	0.1	6.5	3.6
NO_2 ($\mu g\ m^{-3}$)	19.5	12.4	29.1	13.9	-9.6	-1.4	0.5	0.9	-0.3	-0.1	0.3	0.2	9.6	1.4
CO (10 $\mu g\ m^{-3}$)	61.9	30.7	48.7	28.2	13.1	2.5	0.8	0.7	0.3	0.1	0.3	0.1	13.1	2.5
$PM_{2.5}$ ($\mu g\ m^{-3}$)	80.9	32.6	65.7	24.6	15.1	8.1	0.7	0.3	0.2	0.3	0.3	0.3	15.1	8.1

SIM and OBS represent the average of calculated and measured concentrations of chemicals [$\mu g\ m^{-3}$]. Bias is the mean bias [$\mu g\ m^{-3}$]; *R* is the correlation coefficient (unitless); NMB is the normalized mean bias (unitless); NME is the normalized mean error (unitless); RMSE is the root mean square error (unitless).

Table S4. Comparison between values of the maximum and average HONO mixing ratio [Units: ppbv] derived from local observations and calculated by our regional model

Location	Period	Maximum	Mean ± SD	References
Beijing (urban)	January 2016	-	1.05 ± 0.89	Wang et al., (2017)
	June-July 2016	-	1.38 ± 0.90	Wang et al., (2017)
	October 2018	2.50	-	Zhang et al., (2022)
	January 2018	3.00	1.30	This study
	July 2018	2.4	0.89	This study
Shanghai (urban)	Oct. 2004-Jan. 2005	-	1.10 ± 1.0	Cui et al., (2018)
	January 2018	2.40	1.10	This study
	July 2018	0.75	0.55	This study
Guangzhou (urban)	July 2016	-	1.03	Yang et al., (2017)
	Sep.-Nov. 2018	1.50	0.74 ± 0.70	Yu et al., (2022)
	January 2018	3.00	1.20	This study
	July 2018	1.95	1.05	This study
Chengdu (urban)	Aug.-Sep. 2019	2.00	1.3	Yang et al., (2021)
	January 2018	2.60	1.15	This study
	July 2018	2.15	0.95	This study
Wangdu (rural)	June 2018	1.56	-	Liu et al., (2019)
	January 2018	3.12	1.40	This study
	July 2018	2.40	1.00	This study
Heshan (rural)	Oct.-Nov. 2014	1.40	-	Yu et al., (2022)
	January 2018	1.05	0.35	This study
	July 2018	0.35	0.15	This study
Hok Tsui (background)	Sep.-Dec. 2012	-	0.13 ± 0.09	Zha et al., (2014)
	January 2018	0.14	0.06	This study
	July 2018	0.05	0.02	This study

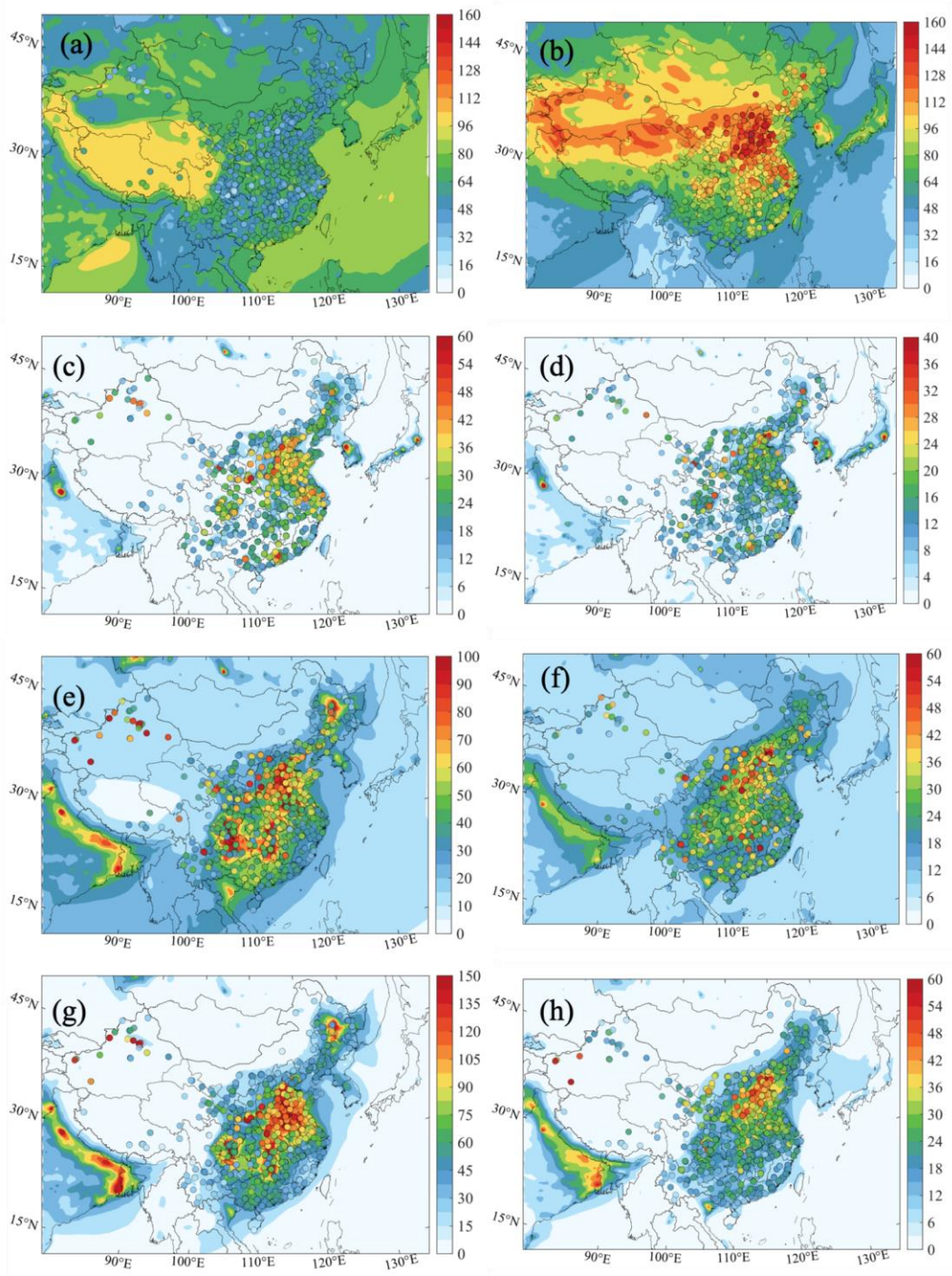

Figure S1. Spatial distribution of the simulated surface maximum daily 8-hour average (MDA8) ozone (a, b) [Unit: μg m^{-3}], monthly average NO_2 (c, d) [Unit: μg m^{-3}], CO (e, f) [Unit: 10 μg m^{-3}], and $PM_{2.5}$ (g, h) [Unit: μg m^{-3}] concentrations. The left column panels are for January and the right column panels are for July 2018. In all cases, the units are μg/m^3. Circles with colors represent observed values at monitoring stations.

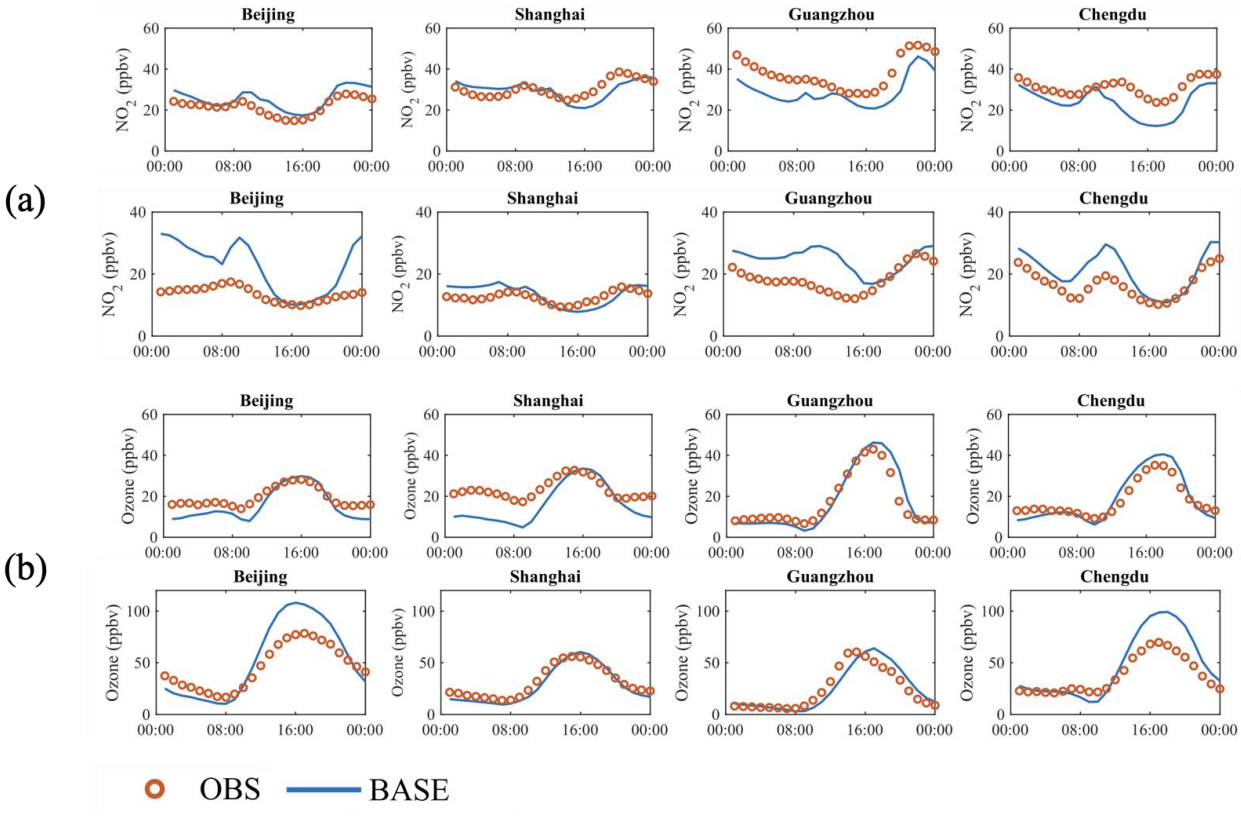

Figure S2. Diurnal variation of observed and simulated mixing ratio [Unit: ppbv] of NO_2 (a) and ozone (b) in four city sites in January (first and third rows) and July (second and fourth rows) of 2018.

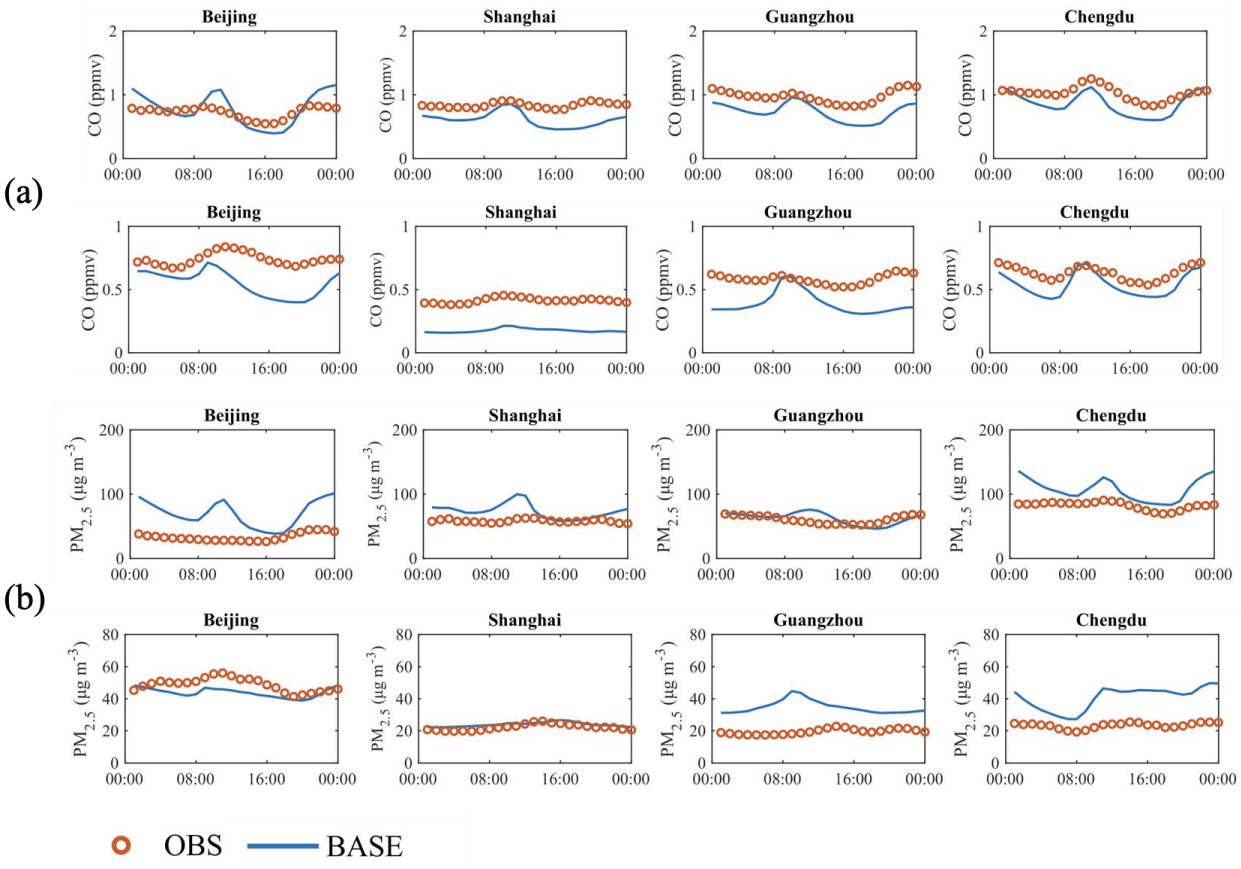

Figure S3. Diurnal variation of observed (circles in orange) and simulated (line in blue) mixing ratio of CO [Unit: ppmv] (a) and $PM_{2.5}$ [Unit: μg m^{-3}](b) in four city sites in January (first and third rows) and July (second and fourth rows) of 2018.

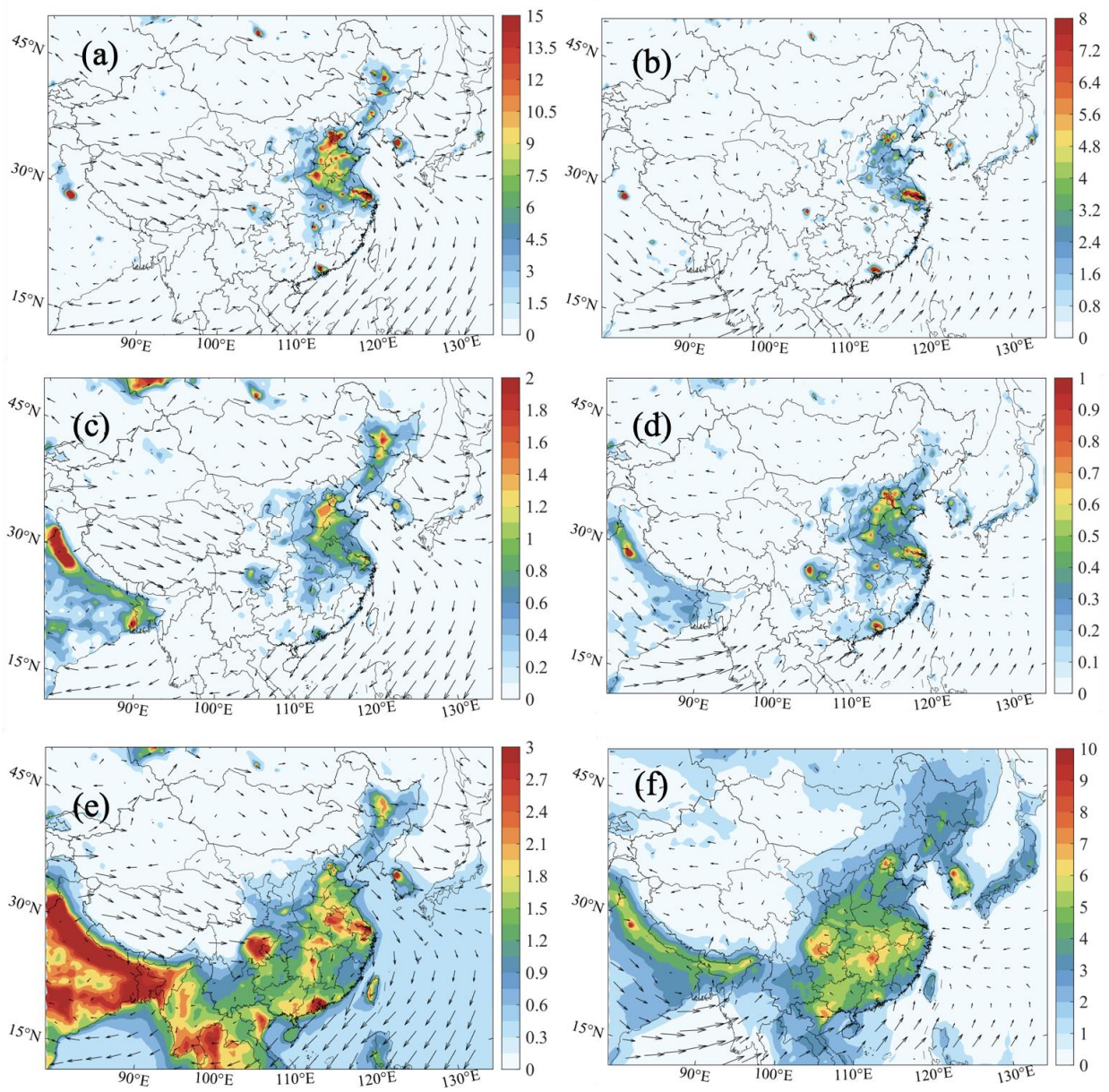

Figure S4. Spatial distribution of the simulated surface mixing ratio [Unit: ppbv] of NO (a, b), HONO (c, d), and HCHO (e, f) average for daytime (08:00-19:00 Local Standard Time (LST)) in January and July 2018.

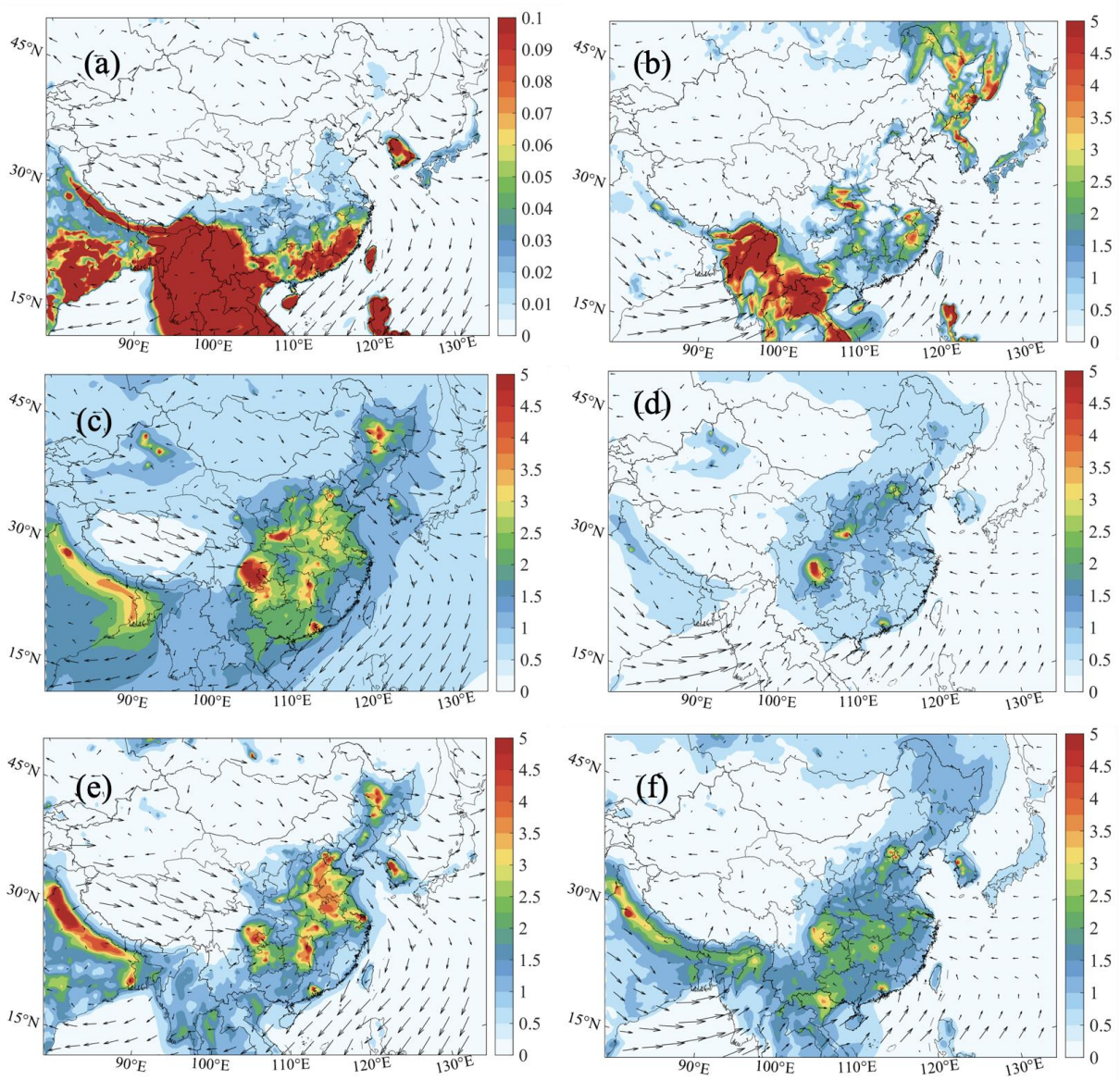

Figure S5. Spatial distribution of simulated mixing ratio [Units: ppbv] of isoprene (a, b), ethene (c, d), and ethane (e, f) average for daytime in January and July 2018.

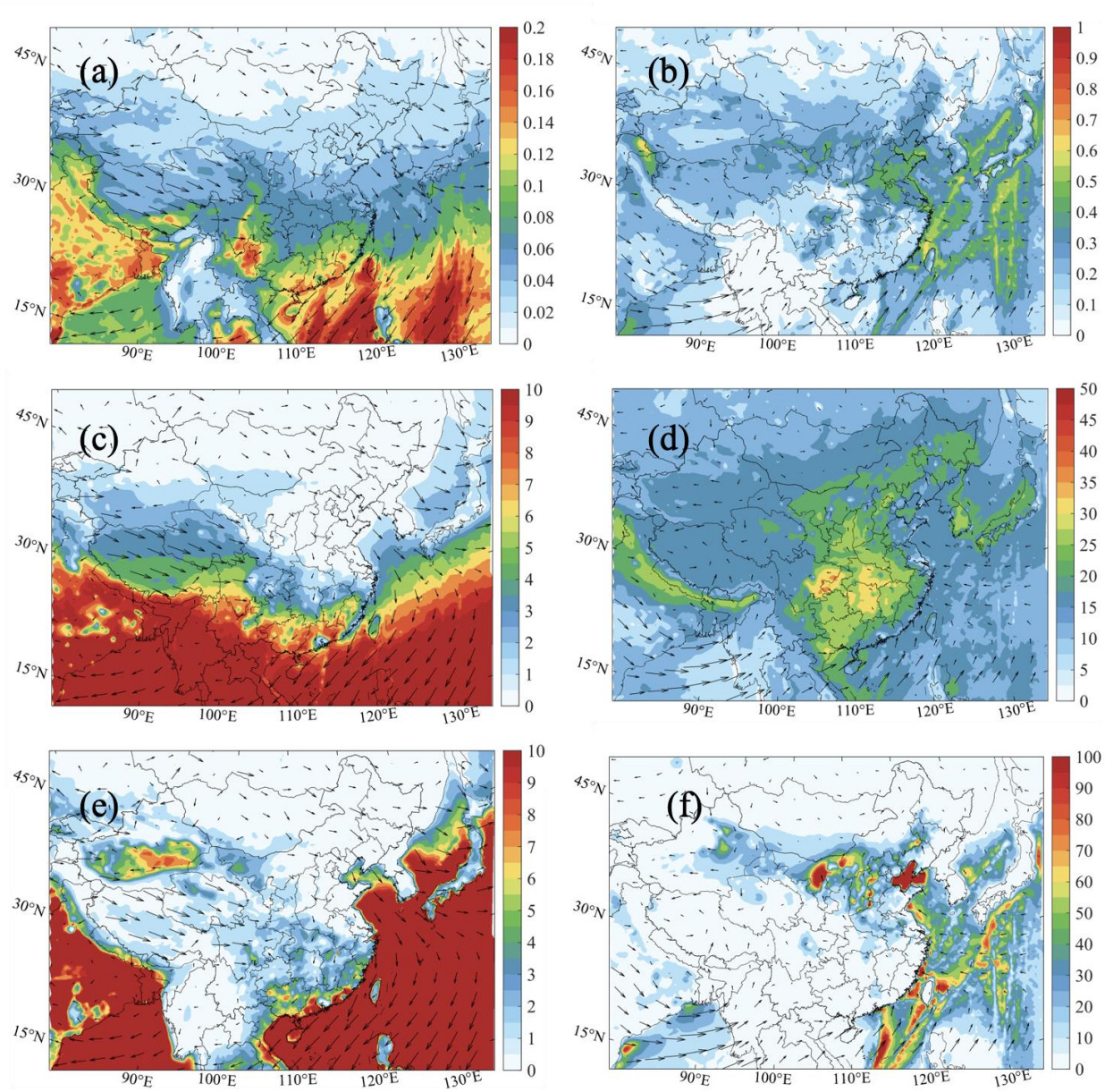

Figure S6. Spatial distribution of simulated surface mixing ratio [Units: pptv] of OH (a, b) and HO_2 (c, d) averaged for daytime and NO_3 (e, f) averaged for nighttime (19:00-06:00 LST) in January and July of 2018.

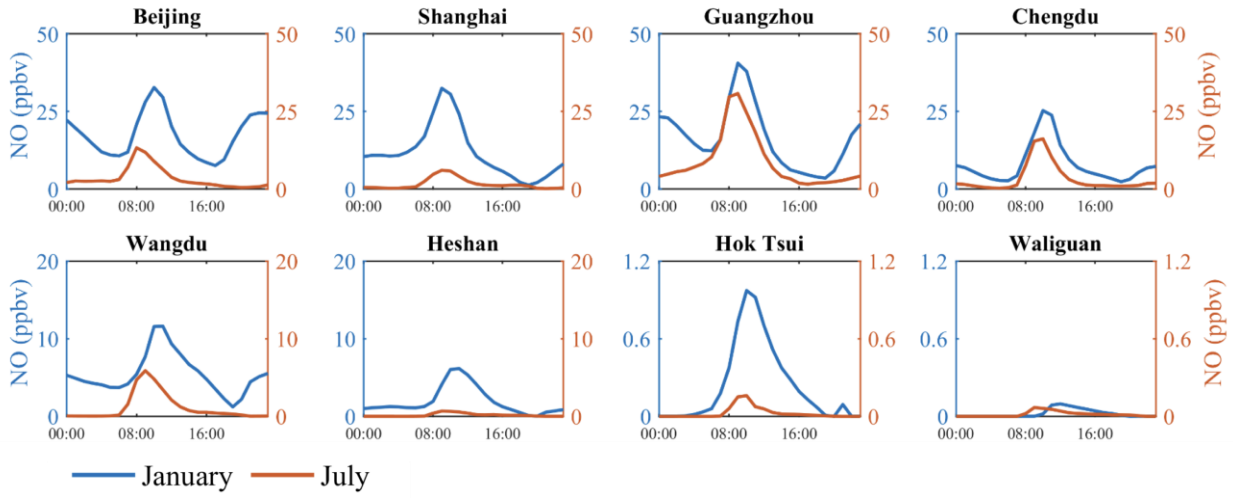

Figure S7. Diurnal variation of the simulated mixing ratio of NO [Unit: ppbv] in different sites in January (in blue, left axis) and July (in orange, right axis) of 2018.

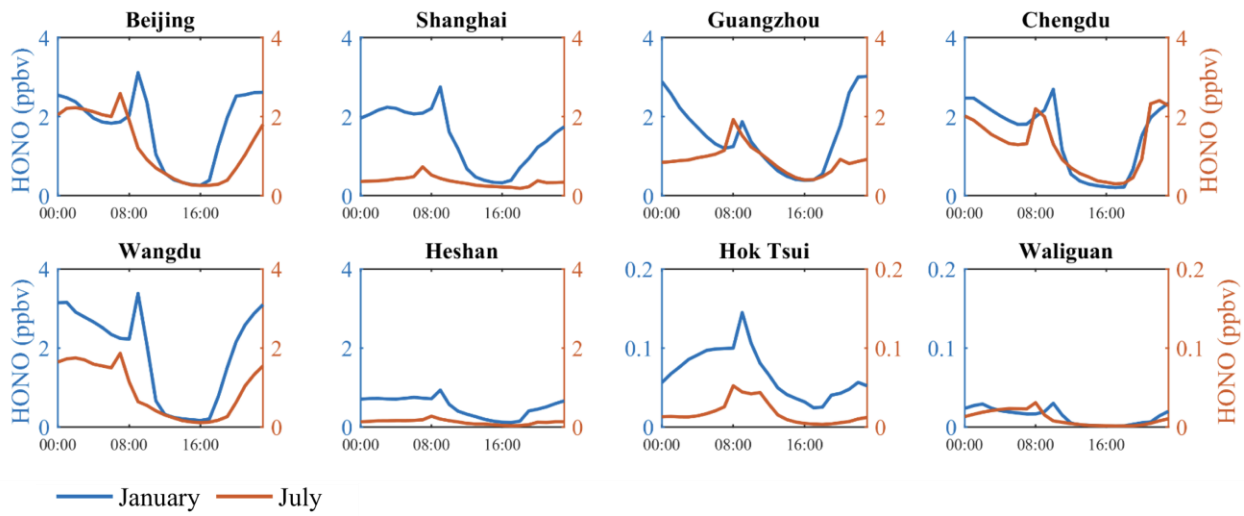

Figure S8. Diurnal variation of the simulated mixing ratio of HONO [Units: ppbv] in different sites in January (in blue, left axis) and July (in orange, right axis) of 2018.

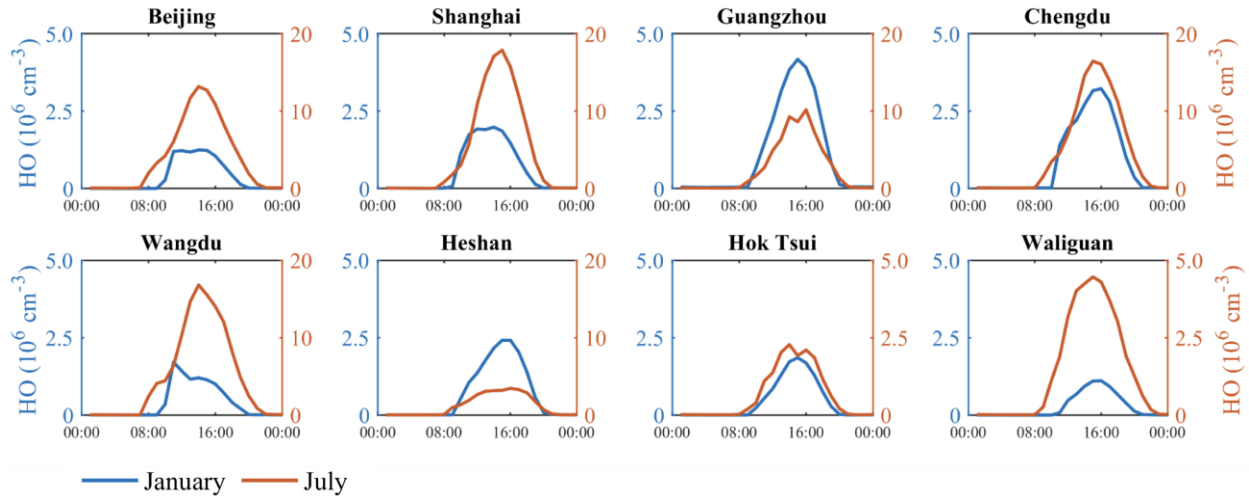

Figure S9. Diurnal variation of simulated mixing ratio [Unit: 10^6 cm^{-3}] of OH radical in different sites in January (in blue, left axis) and July (in orange, right axis) of 2018.

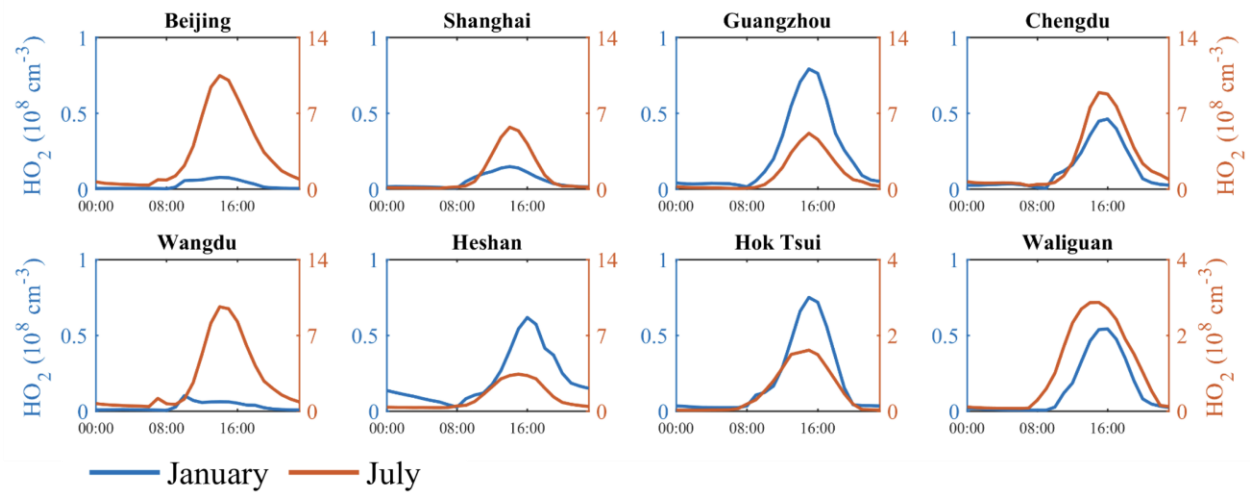

Figure S10. Diurnal variation of simulated mixing ratio [Unit: 10^8 cm^{-3}] of HO_2 radical in different sites in January (in blue, left axis) and July (in orange, right axis) of 2018.

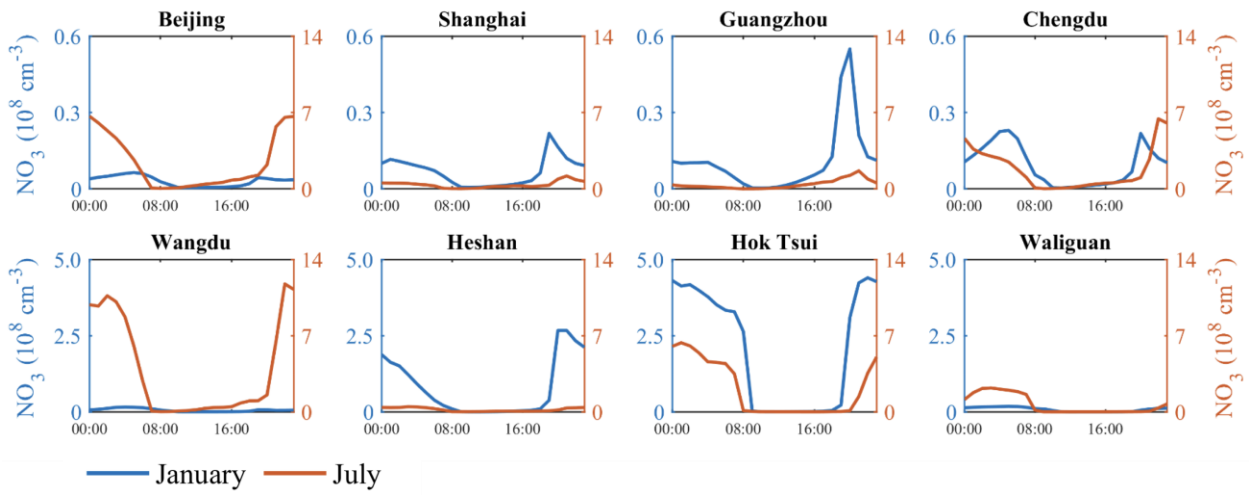

Figure S11. Diurnal variation of simulated mixing ratio [Unit: 10^8 cm^{-3}] of NO_3 radical in different sites in January (in blue, left axis) and July (in orange, right axis) of 2018.

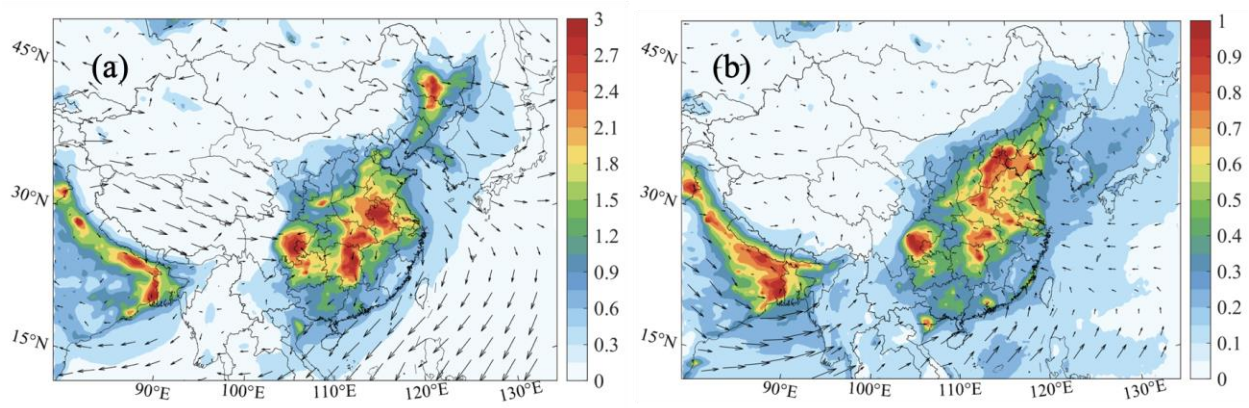

Figure S12. Spatial distribution of the monthly average simulated aerosol surface area density [Unit: 10^{-5} cm^2 cm^{-3}] average in January (a) and July (b), 2018.

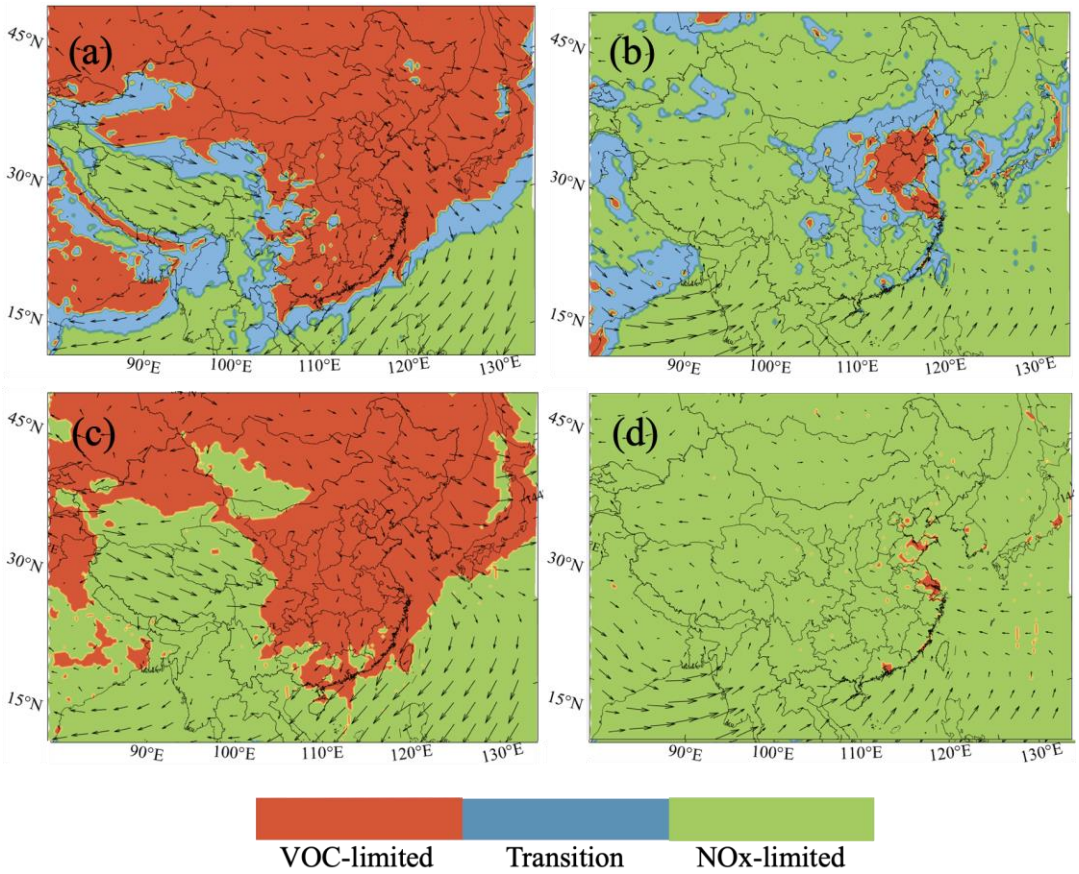

Figure S13. Display of regions in which the ozone production is controlled by the availability of NO_x (green), and VOC (red) in the daytime of January (a, c) and July (b, d). The regions with intermediate conditions are shown in blue. The indicators that are used to define these regions are the concentration ratios between H_2O_2 and HNO_3 (a, b) and the ratio between RO_x losses L_H and L_{NOx} (c, d).

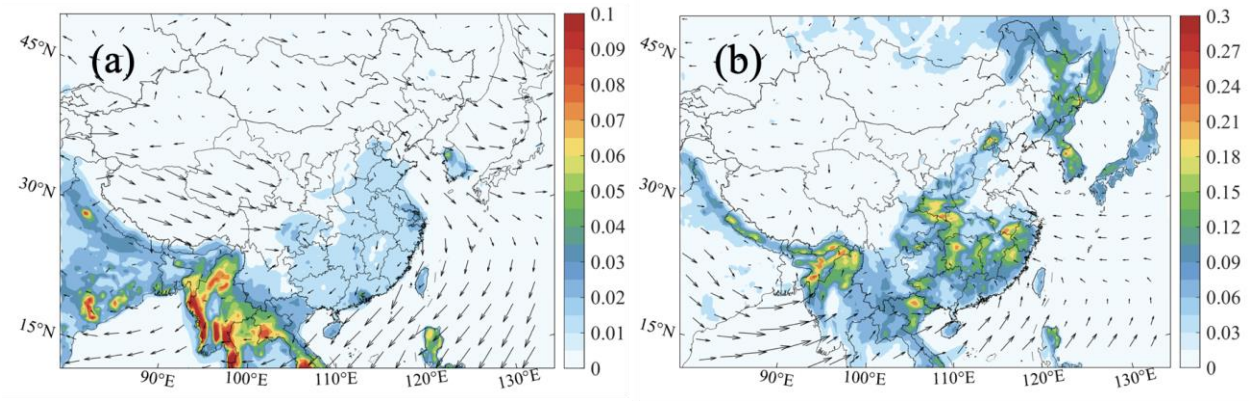

Figure S14. Spatial distribution of production rate of RO_x (RO_2+HO_2+OH) [$P(RO_x)$, Unit: ppbv h^{-1}] (*Het-All* case) from the ozonolysis (Reactions between O_3 and alkene) in the daytime (08:00-19:00 Local Standard Time (LST)) of January (a) and July (b) 2018.

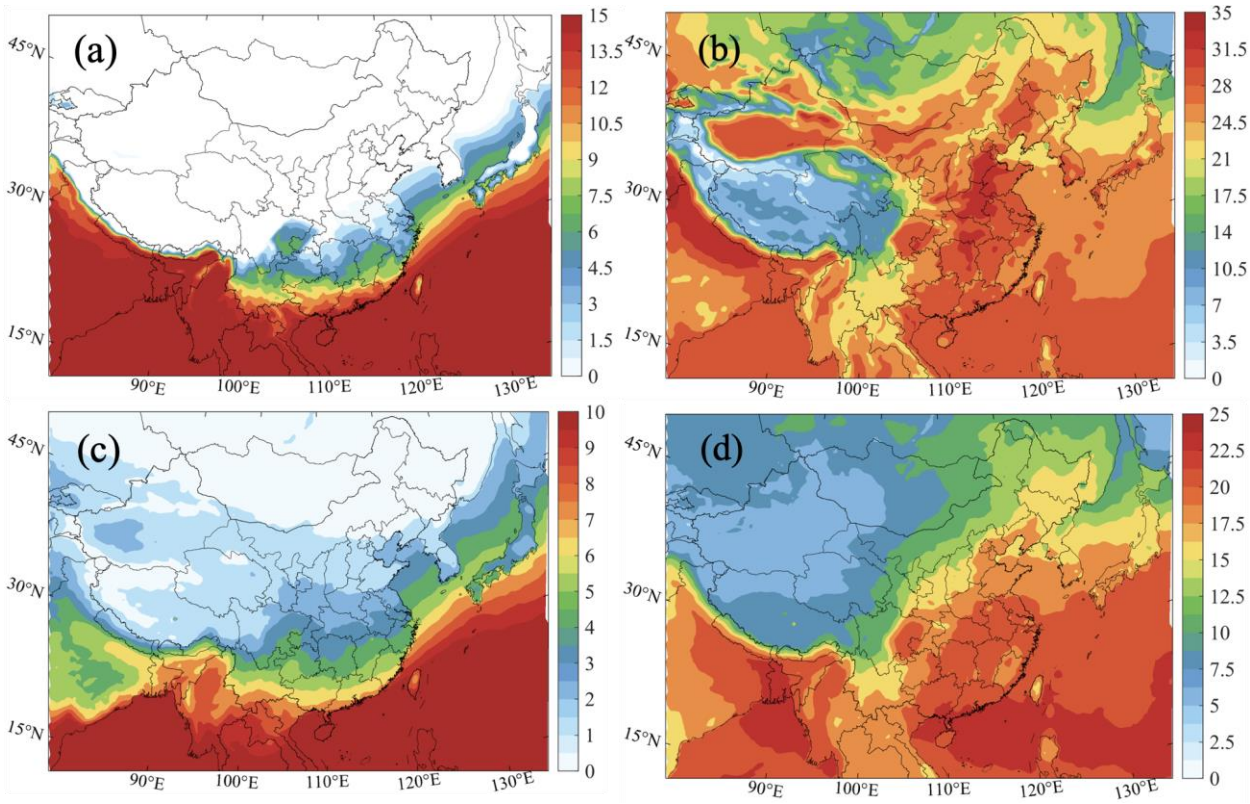

Figure S15. Spatial distribution of surface temperature [Unit: ° C; a, b] and water vapor [Unit: g kg^{-1}; c, d] in the daytime of January (a, c) and July (b, d) from the *Het-All* case.

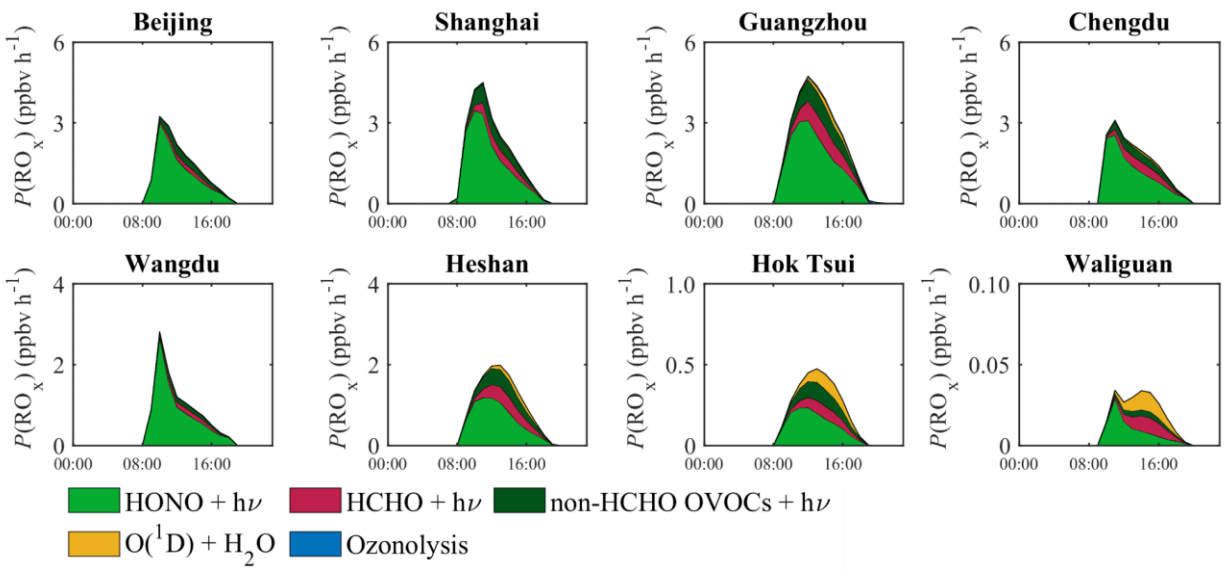

Figure S16. Diurnal variation of simulated production of RO_x (RO_2+HO_2+OH) [Unit: ppbv h^{-1}] in cities and remote sites in January.

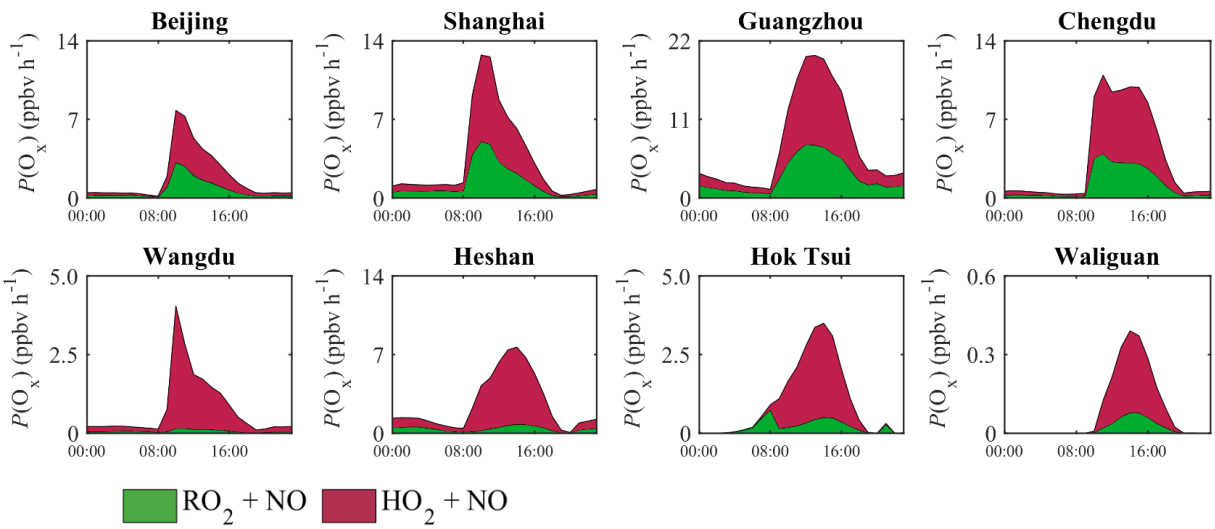

Figure S17. Diurnal variation of simulated O_x production rate [Unit: ppbv h^{-1}] in different regions in January 2018.

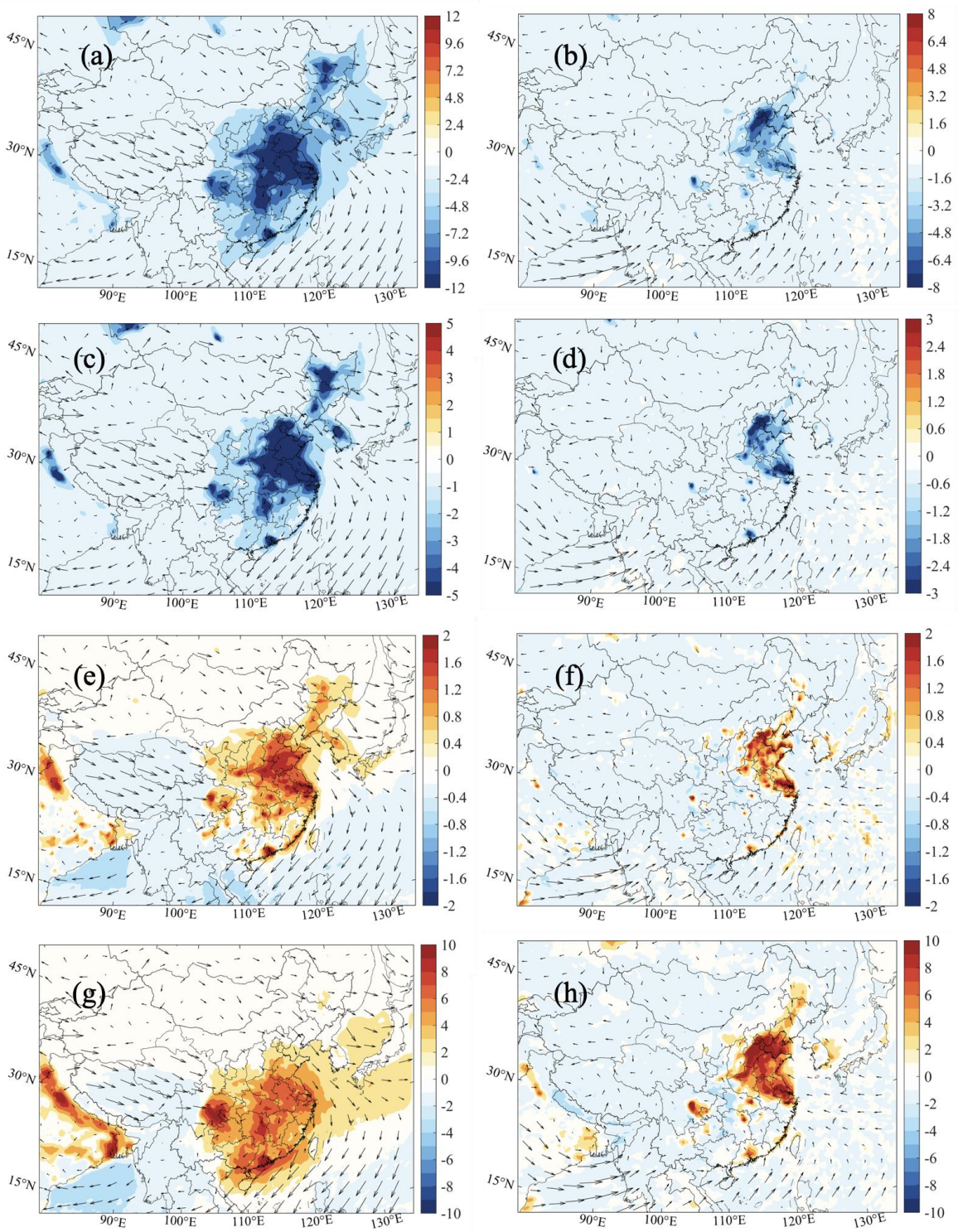

Figure S18. Changes in the surface mixing ratio of NO_2 (a, b) [Unit: ppbv], NO (c, d) [Unit: ppbv], OH (e, f) [Unit: 0.1 pptv], and HO_2 (g, h) [Unit: pptv] resulting from the introduction in the model of on heterogeneous chemical processes on aerosol particles in the daytime (06:00-19:00 LST) of January and July.

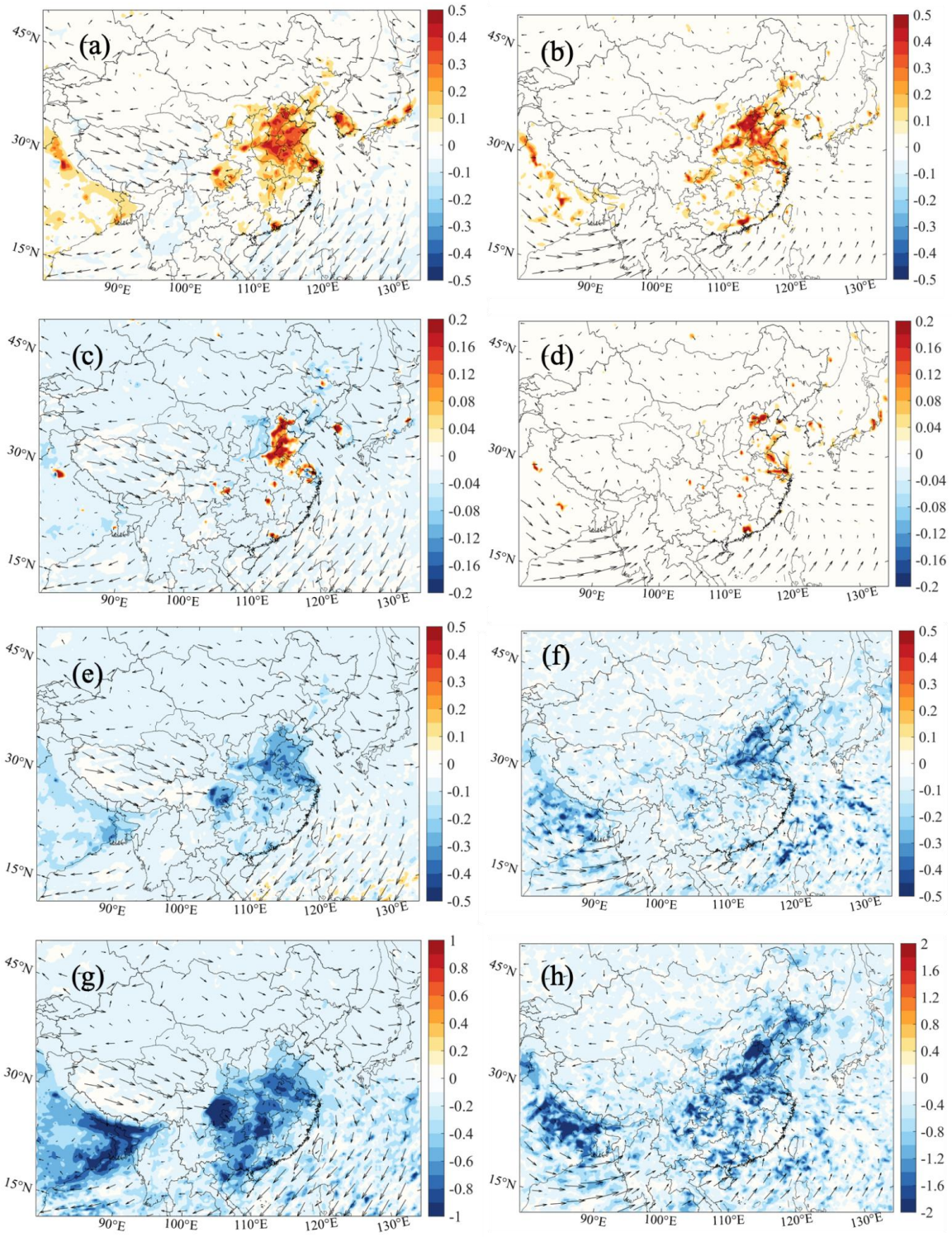

Figure S19. Changes in the surface mixing ratio of NO_2 (a, b) [Unit: ppbv], NO (c, d) [Unit: ppbv], OH (e, f) [Unit: 0.1 pptv] and HO_2 (g, h) [Unit: pptv] resulting from the introduction in the model of aerosol effects on photolysis (increased extinction of solar light) in the daytime (06:00-19:00 LST) of January and July.

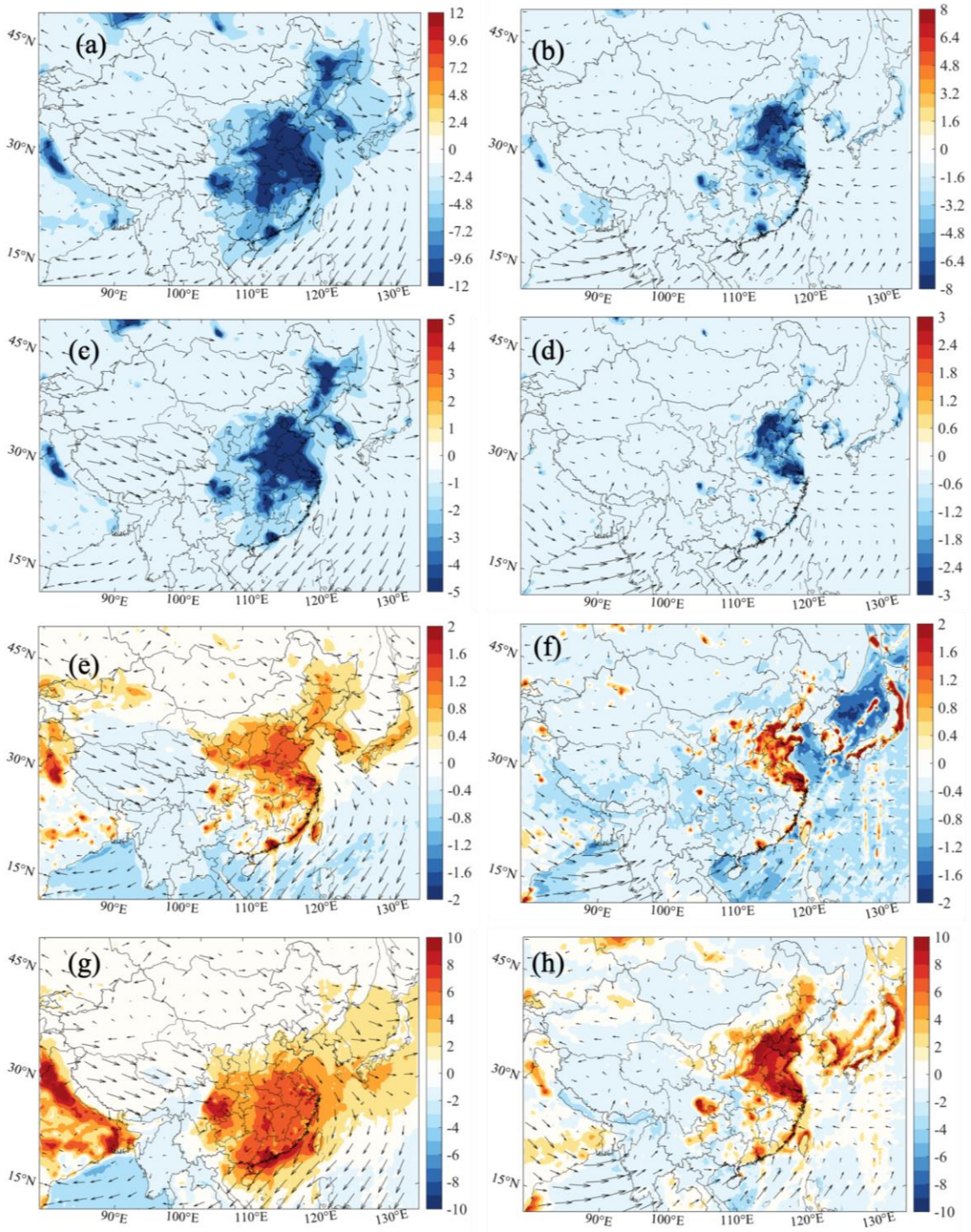

Figure S20. Changes in the surface mixing ratio of NO_2 (a, b) [Unit: ppbv], NO (c, d) [Unit: ppbv], OH (e, f) [Unit: 0.1pptv], and HO_2 (g, h) [Unit: pptv] resulting from the introduction in the model of combined aerosol effects (effect on radiation/photolysis and uptake on particles) in the daytime (06:00-19:00 LST) of January and July.

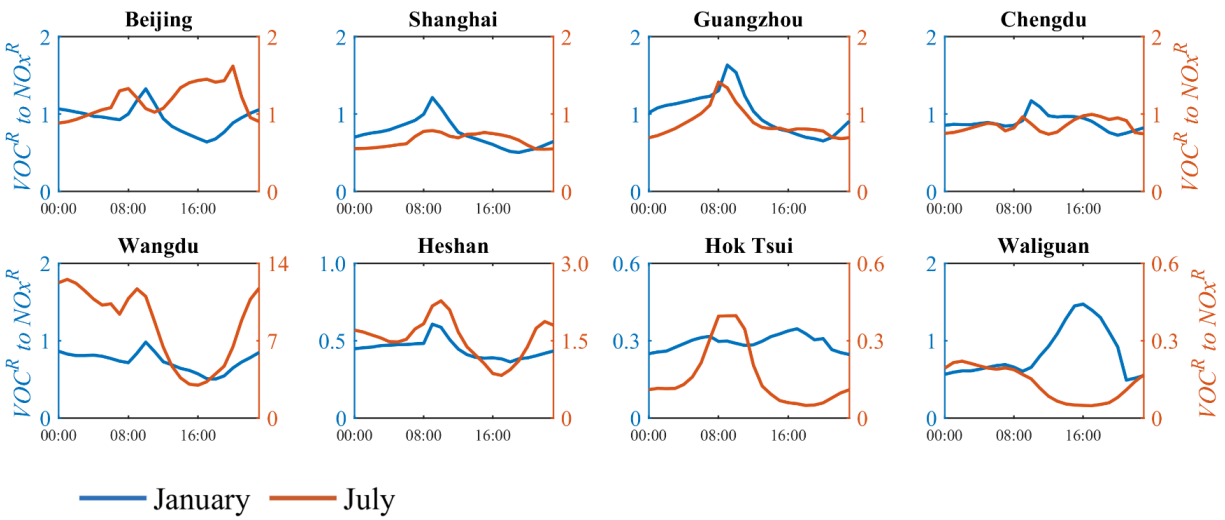

Figure S21. Diurnal variation of the simulated value of the ratio of VOC^{R} and NO_x^{R} in different sites in January (in blue, left axis) and July (in orange, right axis) of 2018.

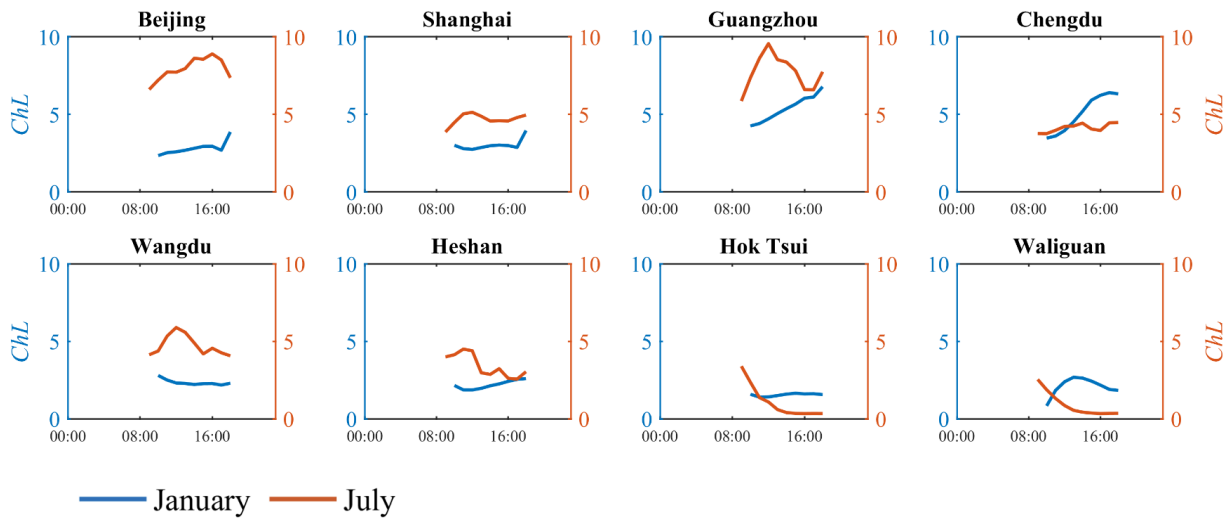

Figure S22. Diurnal variation of *ChL* in different sites in January (in blue, left axis) and July (in orange, right axis) of 2018.

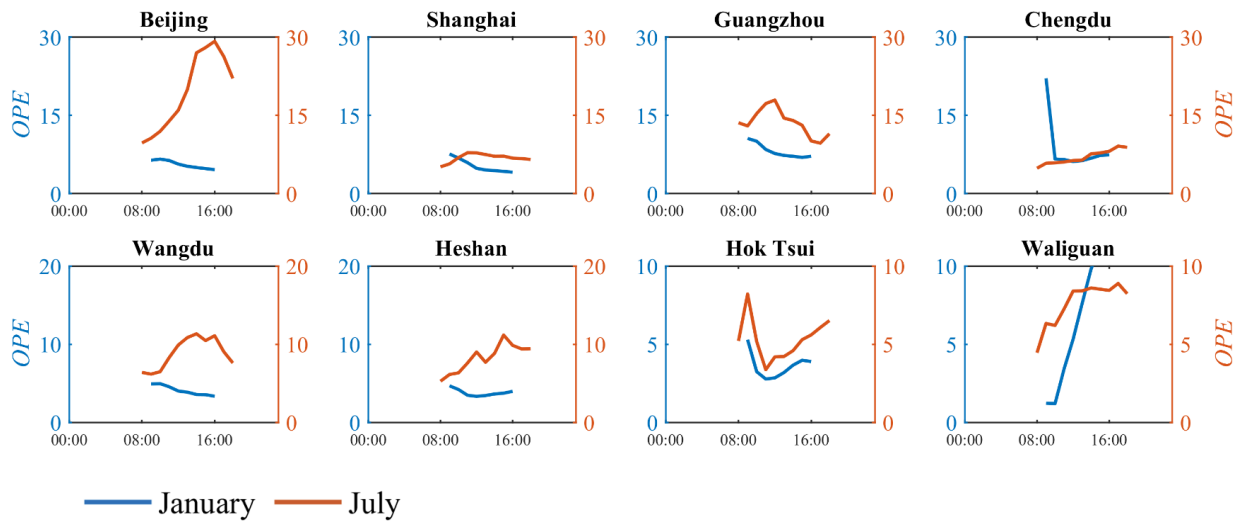

Figure S23. Diurnal variation of *OPE* in different sites in January (in blue, left axis) and July (in orange, right axis) of 2018.

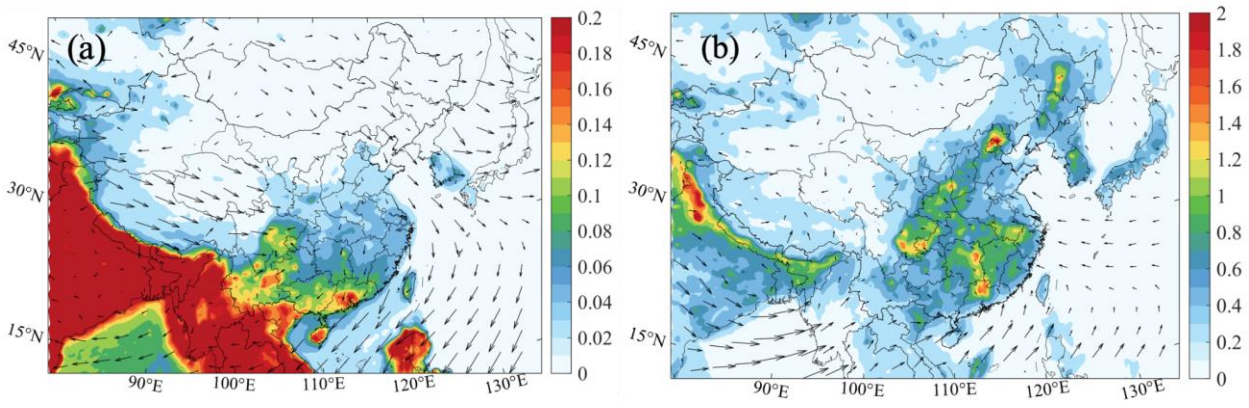

Figure S24. Spatial distribution of nighttime atmospheric oxidation capacity (*AOC* [Unit: 10^7 molecular cm^{-3} s^{-1}]) in January (a) and July(b) of 2018 extracted from the *Het-All* case.

References:

Brown, S. S., Stutz, J. Nighttime radical observations and chemistry. Chemical Society Reviews, 41(19), 6405-6447.https://doi.org/10.1039/C2CS35181A, 2012.

Chen, F., Dudhia, J. Coupling an Advanced Land Surface–Hydrology Model with the Penn State–NCAR MM5 Modeling System. Part I: Model Implementation and Sensitivity, Monthly Weather Review, 129(4), 569-585. https://journals.ametsoc.org/view/journals/mwre/129/4/1520-0493_2001, 2001.

Cui, L., Li, R., Zhang, Y., Meng, Y., Fu, H., Chen, J. An observational study of nitrous acid (HONO) in Shanghai, China: The aerosol impact on HONO formation during the haze episodes. Sci. of the Total Environ., 630, 1057-1070. https://doi.org/10.1016/j.scitotenv.2018.02.063, 2018.

Dai, J., Liu, Y., Wang, P., Fu, X., Xia, M., Wang, T. The impact of sea-salt chloride on ozone through heterogeneous reaction with N2O5 in a coastal region of south China. Atmospheric environment, 236, 117604. https://doi.org/10.1016/j.atmosenv.2020.117604, 2020.

Emmons, L. K., Walters, S., Hess, P. G., Lamarque, J.-F., Pfister, G. G., Fillmore, D., Granier, C., Guenther, A., Kinnison, D., Laepple, T., Orlando, J., Tie, X., Tyndall, G., Wiedinmyer, C., Baughcum, S. L., and Kloster, S.: Description and evaluation of the Model for Ozone and Related chemical Tracers, version 4 (MOZART-4), Geosci. Model Dev., 3, 43–67, https://doi.org/10.5194/gmd-3-43-2010, 2010.

Grell, G. A., and Dévényi, D., A generalized approach to parameterizing convection combining ensemble and data assimilation techniques, Geophys. Res. Lett., 29(14), doi:10.1029/2002GL015311, 2002.

Hong, S., Noh, Y., and Dudhia, J. . A New Vertical Diffusion Package with an Explicit Treatment of Entrainment Processes. Monthly Weather Review 134, 9, 2318-2341,https://doi.org/10.1175/MWR3199.1, 2006.

Liu, Y., Lu, K., Li, X., Dong, H., Tan, Z., Wang, H., Zhang, Y. A comprehensive model test of the HONO sources constrained to field measurements at rural North China Plain. Environmental science & technology, 53(7), 3517-3525. https://doi.org/10.1021/acs.est.8b06367, 2019.

Ma, X., Tan, Z., Lu, K., Yang, X., Liu, Y., Li, S., Zhang, Y, Winter photochemistry in Beijing: Observation and model simulation of OH and HO2 radicals at an urban site. Sci. of the Total Environ., 685: 85-95, https://doi.org/10.1016/j.scitotenv.2019.05.329, 2019.

Madronich, S. Photodissociation in the atmosphere: 1. Actinic flux and the effects of ground reflections and clouds. Journal of Geophysical Research: Atmospheres, 92(D8), 9740-9752. https://doi.org/10.1029/JD092iD08p09740, 1987.

Mlawer, E. J., Taubman, S. J., Brown, P. D., Iacono, M. J., and Clough, S. A. Radiative transfer for inhomogeneous atmospheres: RRTM, a validated correlated-k model for the longwave, J. Geophys. Res., 102(D14), 16663– 16682, https://doi.org/10.1029/97JD00237, 1997.

Morrison, H. C. J. A., J. A. Curry, and V. I. Khvorostyanov. "A new double-moment microphysics parameterization for application in cloud and climate models. Part I: Description." Journal of the atmospheric sciences 62.6: 1665-1677. https://doi.org/10.1175/JAS3446.1, 2005.

Tan, Z., Fuchs, H., Lu, K., Hofzumahaus, A., Bohn, B., Broch, S., Zhang, Y. Radical chemistry at a rural site (Wangdu) in the North China Plain: observation and model calculations of OH, HO_2 and RO_2 radicals. Atmos. Chem. Phys., 17(1), 663-690., https://doi.org/10.5194/acp-17-663-201, 2017.

Tie, X., Madronich, S., Walters, S., Zhang, R., Racsh, P., and Collins, W., Effect of clouds on photolysis and oxidants in the troposphere, J. Geophys. Res., 108, 4642, https://doi.org/10.1029/2003JD003659, 2003.

Wang, H., Wang, H., Lu, X., Lu, K., Zhang, L., Tham, Y. J., Zhang, Y. Increased night-time oxidation over China despite widespread decrease across the globe. Nature Geoscience, 1-7. https://doi.org/10.1038/s41561-022-01122-x, 2023.

Wang, P., Liu, Y., Dai, J., Fu, X., Wang, X., Guenther, A., Wang, T. Isoprene emissions response to drought and the impacts on ozone and SOA in China. Journal of Geophysical Research: Atmospheres, 126, e2020JD033263. https://doi.org/10.1029/2020JD033263, 2021.

Wang T, Xue L, Brimblecombe P, Lam YF, Li L, Zhang L. Ozone pollution in China: A review of concentrations, meteorological influences, chemical precursors, and effects. Sci Total Environ. 575:1582-1596. https://doi.org/10.1016/j.scitotenv.2016.10.081, 2017.

Yang, W., Cheng, P., Tian, Z., Zhang, H., Zhang, M., & Wang, B. (2017). Study on HONO pollution characteristics and daytime unknown sources during summer and autumn in Guangzhou, China. China Environmental Science, 37(6), 2029-2039.

Yang, X., Lu, K., Ma, X., Liu, Y., Wang, H., Hu, R., Zhang, Y. Observations and modeling of OH and HO2 radicals in Chengdu, China in summer 2019. Science of The Total Environment, 772, 144829.https://doi.org/10.1016/j.scitotenv.2020.144829, 2021.

Yang, Y., Li, X., Zu, K., Lian, C., Chen, S., Dong, H., Zhang, Y. Elucidating the effect of HONO on O3 pollution by a case study in southwest China. Science of The Total Environment, 756, 144127.https://doi.org/10.1016/j.scitotenv.2020.144127, 2021.

Yang, X., Lu, K., Ma, X., Gao, Y., Tan, Z., Wang, H., Zhang, Y. Radical chemistry in the Pearl River Delta: observations and modeling of OH and HO2 radicals in Shenzhen in 2018. Atmos. Chem. Phys., 22(18), 12525-12542. https://doi.org/10.5194/acp-22-12525-2022, 2022.

Yu, Y., Cheng, P., Li, H., Yang, W., Han, B., Song, W., ... & Yu, X. (2021). Budget of nitrous acid (HONO) and its impacts on atmospheric oxidation capacity at an urban site in the fall season of Guangzhou, China. Atmos. Chem. Phys. Discuss, https://doi.org/10.5194/acp-22-8951-2022, in review.

Zaveri, R. A., Easter, R. C., Fast, J. D., and Peters, L. K., Model for Simulating Aerosol Interactions and Chemistry (MOSAIC), J. Geophys. Res., 113, D13204, https://doi.org/10.1029/2007JD008782, 2008.

Zha, Q., Xue, L., Wang, T., Xu, Z., Yeung, C., Louie, P. K. K., and Luk, C. W. Y. Large conversion rates of NO_2 to HNO_2 observed in air masses from the South China Sea: Evidence of strong production at sea surface? Geophys. Res. Lett., 41, 7710– 7715, https://doi.org/10.1002/2014GL061429, 2014.

Zhang, J., Lian, C., Wang, W., Ge, M., Guo, Y., Ran, H., An, J. Amplified role of potential HONO sources in O3 formation in North China Plain during autumn haze aggravating processes. Atmos. Chem. Phys., 22(5), 3275-3302, https://doi.org/10.5194/acp-22-3275-2022, 2022.